University of South Australia

The Library
www.library.unisa.edu.au

Educating Professionals, Creating and Applying Knowledge, Engaging our Communities

NOTICE: this is the accepted author manuscript (AAM) or post-print which was accepted for publication in *Powder Technology*. Changes resulting from the publishing process, such as peer review, editing, corrections, structural formatting, and other quality control mechanisms are reflected in this document. This version is licensed under a Creative Commons CC-BY-NC-ND 4.0 license (http://creativecommons.org/licenses/by-nc-nd/4.0/).

A definitive version was subsequently published in *Powder Technology*, vol. 308, pp. 178-192, 2017, DOI: dx.doi.org/10.1016/j.powtec.2016.11.044

Powder Technology 308 (2017) 178–192

Contents lists available at ScienceDirect

Powder Technology

journal homepage: www.elsevier.com/locate/powtec

The gas-solid flow characteristics of cyclones

Jianping Wei [a,*], Hongtu Zhang [a], Yungang Wang [b], Zhihui Wen [a], Banghua Yao [a], Jianghui Dong [c,*]

[a] State Key Laboratory Cultivation Base for Gas Geology and Gas Control, School of Safety Science and Engineering, Henan Polytechnic University, Jiaozuo 454000, Henan, China
[b] Coal Production Safety Collaborative Innovation Center in Henan Province, Jiaozuo 454000, Henan, China
[c] School of Natural and Built Environments, University of South Australia, Adelaide, SA 5095, Australia

ARTICLE INFO

Article history:
Received 23 July 2016
Received in revised form 8 November 2016
Accepted 26 November 2016
Available online 7 December 2016

Keywords:
Cyclone
Gas-solid flow
Solid gas ratio
Pressure drop

ABSTRACT

Cyclones have been widely used as separation devices during pneumatic conveying. The pipelines and cyclones inlet are connected by diameter change joints. The inlet cross section area is always larger than the pipeline. This results in the velocity of gas becoming lower than particle velocity when the gas-particles flow into the cyclone. The gas-solid flow in cyclones are investigated using FLUENT-EDEM method. The results show that the existence of particles had major effects on the gas flow of the cyclone within the inlet and conical separation parts. The tangential, axial, and radial velocities are only slightly changed when solid gas ratio at the same gas velocity/particle velocity ratio, while the velocities increase with the increasing of gas velocity/particle velocity ratios under the same solid gas ratio. The cyclone pressure drop decreases at a low solid gas ratio, and is maintained at an almost constant level with the high solid gas ratio. However, with the lower solid gas ratio, the particle strands are not clear, and the particle strand is found to become clearer and remained constant when the solid gas ratio is 6.42 kg/kg at the same gas velocity/particle velocity ratio. The particle strands form early with the increasing of gas velocity/particle velocity ratios at the same solid gas ratio. At the same time, the particle-wall interaction force is determined to be the main reason for the particle breakage and wall attrition. The results could potentially provide support for the development of a pressure drop theory for cyclones.

© 2016 Elsevier B.V. All rights reserved.

1. Introduction

Cyclones have been widely used as separation devices for dust or products during pneumatic conveying processes. Generally speaking, a cyclone includes five parts: the inlet, cylindrical, conical, dust out, and vortex finder. A pipeline is connected with the cyclone inlet using a diameter changed joint. Since the inlet cross section area is always larger than the pipeline, this results in the gas velocity becoming lower than the particle velocity when the gas-particles flow into the cyclone. Then, the gas-solid flow induces particle breakage and wall attrition. The particle breakage reduces the particle grade, especially for the lower strength particles. The wall attrition results in a short cyclone life, which leads to increased cost. Therefore, particle breakage and wall attrition are difficult problems, which are faced in cyclone applications and designs.

Experimental [1–5] and theoretical studies [6–11] are the two main methods used to examine the gas-solid flow in a cyclone. The recent studies regarding the gas-solid flow in cyclones have mainly focused on the particle velocity being lower than the gas velocity. However, to date there has been insufficient detailed study conducted regarding the particle velocity being higher than the gas velocity. The experimental studies have been unable capture the entire gas-solid flow structure in a cyclone due to the strong swirling flow. However, simulation studies have overcome the experimental shortcomings [12]. Boysan et al. [13] first adopted a k-ε model to simulate the gas-solid flow in a cyclone. However, this model was built based on the isotropy. The results showed exceedingly higher turbulent viscosity, and inaccurate tangential and axial velocities [14]. In recent studies, the large eddy simulation is verified to be successful to describe the gas flow in cyclone [15–18] and the results are more accurate than other turbulence models [18]. However, large eddy simulation was time consuming [19,20], thus leads to the large eddy simulation has not been widely applied. Other studies have shown that an RSM (Reynolds Stress Model) was suitable to describe the strong swirling gas-solid flow. This model was built based on the anisotropy [21], and the pressure drop and flow characteristics were found to be in good agreement with the experiment results [11,12]. Thus, compared with the large eddy simulation, the RSM was not the best choice to describe the flow in cyclone, but it was still an economic and reliable one. A DPM (Discrete Phase Model) has been widely applied to describe the particle flow when the solid volume fraction was less than 10% [9,22–25]. The DPM took a single particle as the object, and ignored the particle-particle collision. However, when the particle diameter was larger than 0.1 mm, the DPM results were found to be inaccurate [26].

* Corresponding authors at: University of South Australia, School of Natural and Built Environments, Mawson Lakes Campus, Adelaide, South Australia 5095, Australia.
E-mail addresses: hpuwjp@163.com (J. Wei), jianghui.dong@mymail.unisa.edu.au (J. Dong).

http://dx.doi.org/10.1016/j.powtec.2016.11.044
0032-5910/© 2016 Elsevier B.V. All rights reserved.

With the development of computer technology and discrete element methods (DEM), Tsuji [27] first presented and applied a CFD-DEM coupling simulation to study gas-solid flow. In recent studies, this method has been successfully applied in fluidized beds [28,29], oil drilling [30], and mineral separation [31]. Siamak [30] studied drill-cutting flows using FLUENT-EDEM coupling simulations. Mohammadreza [32] and Zhou [33] both adopted FLUENT-EDEM coupling simulations to study gas-solid flows, and their results were in agreement with the experimental results. The FLUENT-EDEM coupling simulations were also determined to suitable to describe the gas-solid flow in cyclones.

Based on the negative pressure pneumatic conveying, the sampling method was applied to determine the coal seam gas content. Cyclone was adopted as the coal sample collector. For the restriction of application conditions, the cross section area of cyclone inlet was about 3.2 times as that of conveying pipeline. When the gas velocity was 20 m/s in the conveying pipeline, and the velocity was reduced at ~6 m/s in the cyclone inlet. The particle still kept steady flow velocity 16 m/s, thus led to a gas-solid flow with higher particle velocity than gas velocity. For the gas velocity was relatively stable, so the ratio between the particle velocity and gas velocity was steady as well.

The particle breakage or attrition in cyclone was inevitable [34,35], which had a disadvantage on the determination of coal seam gas content accurately. The particle breakage or attrition should be reduced. In recent studies, researchers have paid more attention on the gas-solid flow with gas velocity not less than that of particle in cyclone [10–12]. There was insufficient study on the gas-solid flow with higher particle velocity than gas velocity.

Therefore, to meet the demand of the application of negative pressure pneumatic conveying for determining the gas content, and provide the supplement for the gas-solid flow in cyclone, it is necessary to carry out the study about the gas velocity is lower than particle velocity.

In this study, the gas-solid flow in cyclones was investigated using FLUENT15.0 (ANSYS, Inc. PA, USA)-EDEM2.7 (DEM Solutions Ltd., Edinburgh, United Kingdom) coupling simulations. The primary aim was to capture the gas flow characteristics, as well as the particle-particle and particle-wall interactions when the particle velocity was higher than the gas velocity. The results could potentially reveal the underlying causes of particle breakage and cyclone wall attrition. The present study could also potentially provide support for diameter changed joint design, along with improvements in cyclone theory and use efficiency.

2. Materials and methods

2.1. Mathematical model

2.1.1. Particle motion governing equations

In the FLUENT-EDEM, a single particle was described based on the Second Newton's Law. Particle i could then be described as follows [36]:

$$F_i = m_i \ddot{v}_i \tag{1}$$

$$M_i = I_i \ddot{\theta}_i \tag{2}$$

where $\ddot{v}_i$ and $\ddot{\theta}_i$ are the acceleration velocity and angular acceleration of particle i, respectively; m_i and I_i are the particle mass and moment of inertia of particle i, respectively; and F_i and M_i are the total force and total torque, respectively.

The EDEM package provided several contact models to describe the particle-particle and particle-wall interactions. In this study, a Hertz-Mindlin no slip contact model was selected [30]. The contact model is described in Fig. 1.

In the gas-solid flow within a cyclone, some forces were found to be acting on the particles, such as drag, gravity, particle-particle interactions, Buoyance, pressure gradient, Magnus, virtual mass, and so on. However, the pressure gradient, Magnus, and virtual mass forces were minimal and could be ignored. Therefore, the forces acting on the particles could be described as follows [36,37]:

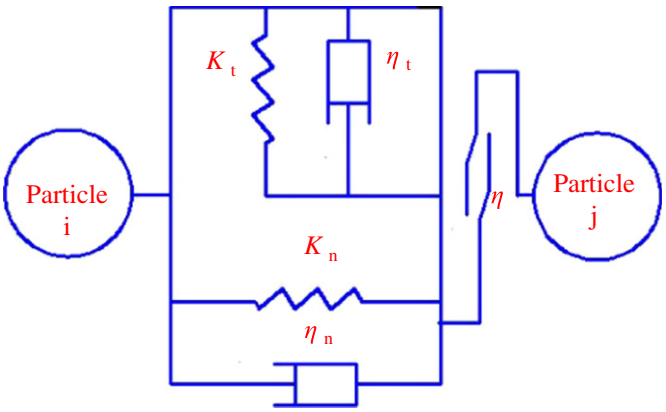


Fig. 1. Scheme of contact model.

$$F_i = m_i g + f_{p-g,i} + \sum_{j=1}^{k_i} \left(f_{c,ij} + f_{d,ij} \right) \tag{3}$$

where $f_{p-g,i}$ represents the drag force acting on the particles; $f_{c,ij}$ is the contact force between particles i and j; and $f_{d,ij}$ is the damping force between particles i and j.

An Ergun-Wen-Yu drag force model [38] was adopted to describe the $f_{p-g,i}$.

$$f_{c,ij} = f_{n,ij}^{c} + f_{t,ij}^{c} \tag{4}$$

$$f_{n,ij}^{c} = \frac{4}{3} E^* \sqrt{R^*} \delta_n^{\frac{3}{2}} \tag{5}$$

$$f_{t,ij}^{c} = -2\sqrt{\frac{5}{6}} \beta \sqrt{S_n m^*} v_n^{rel} \tag{6}$$

$$\beta = \frac{\ln e}{\sqrt{\ln^2 e + \pi^2}} \tag{7}$$

$$S_n = 2Y^* \sqrt{R^* \delta_n} \tag{8}$$

where $f_{n,ij}^{c}$ and $f_{t,ij}^{c}$ are the normal contact and tangential contact forces, respectively; E^* is the equivalent Buoyance module; R^* is coal the particle equivalent radius; δ_n represents the normal overlap; m^* is the equivalent mass; v_n^{rel} is the relative normal velocity; e represents the restitution coefficient; s_n is the normal stiffness; and β is the damping coefficient.

$$f_{d,ij} = f_{n,ij}^{d} + f_{t,ij}^{d} \tag{9}$$

$$f_{n,ij}^{d} = -s_t \delta_t \tag{10}$$

$$s_t = 8G^* \sqrt{R^* \delta_n} \tag{11}$$

$$f_{t,ij}^{d} = -2\sqrt{\frac{5}{6}} \beta \sqrt{s_t m^*} v_t^{rel} \tag{12}$$

where $f_{t,ij}^{d}$ and $f_{n,ij}^{d}$ are the tangential damping and normal damping forces, respectively; v_t^{rel} is the relative tangential velocity; s_t is the tangential stiffness; $f_{n,ij}^{d}$ represents the tangential damping force; and G^* is the equivalent shear module.

According to the discrete element method, the rolling friction torque should be considered, and therefore was described as follows:

$$T_i = -\mu_t F_n R_i \omega_i \tag{13}$$

where μ_t is the rolling friction coefficient; F_n is the particle-wall normal contact force; R_i represents the distance from the particle center to the contact face; and ω_i is the particle angle velocity at the contact face.

2.1.2. Gas flow governing equations

During the FLUENT-EDEM coupling simulation, the flow obeyed the mass and momentum conservation laws, and the conservation of the mass and momentum could be described as follows [30]:

$$\frac{\partial\left(\alpha\rho_f\right)}{\partial t} + \nabla\cdot\left(\alpha\rho_f u_f\right) = 0 \tag{14}$$

$$\frac{\partial\left(\alpha\rho_f u_f\right)}{\partial t} + \nabla\cdot\left(\alpha\rho_f u_f u_f\right) = -\alpha\nabla p + \alpha\nabla\cdot\tau - S_f + \alpha\rho_f g \tag{15}$$

where α, ρ_f, u_f, τ, and S_f represented the gas phase volume, gas density, gas velocity, viscous stress tensor, and mean force in the computation cell, respectively.

A Reynolds Stress Turbulence Model was adopted to describe the strong swirling gas flow in a cyclone [39,40].

$$u_k\frac{\partial\left(\overline{u_i' u_j'}\right)}{\partial x_k} = D_{ij} + P_{ij} + \phi_{ij} - \epsilon_{ij} \tag{16}$$

$$D_{ij} = -\frac{\partial}{\partial x_k}\left(\frac{\mu_t}{\sigma_k}\frac{\partial\overline{u_i' u_j'}}{\partial x_k}\right) \tag{17}$$

$$P_{ij} = -\rho\left(\overline{u_i' u_k'}\frac{\partial u_j}{\partial x_k} + \overline{u_j' u_k'}\frac{\partial u_i}{\partial x_k}\right) \tag{18}$$

$$\phi_{ij} = P\left(\overline{\frac{\partial u_i'}{\partial x_j}} + \overline{\frac{\partial u_j'}{\partial x_i}}\right) \tag{19}$$

$$\epsilon_{ij} = 2\mu\overline{\frac{\partial u_i'}{\partial x_j}\frac{\partial u_j'}{\partial x_i}} \tag{20}$$

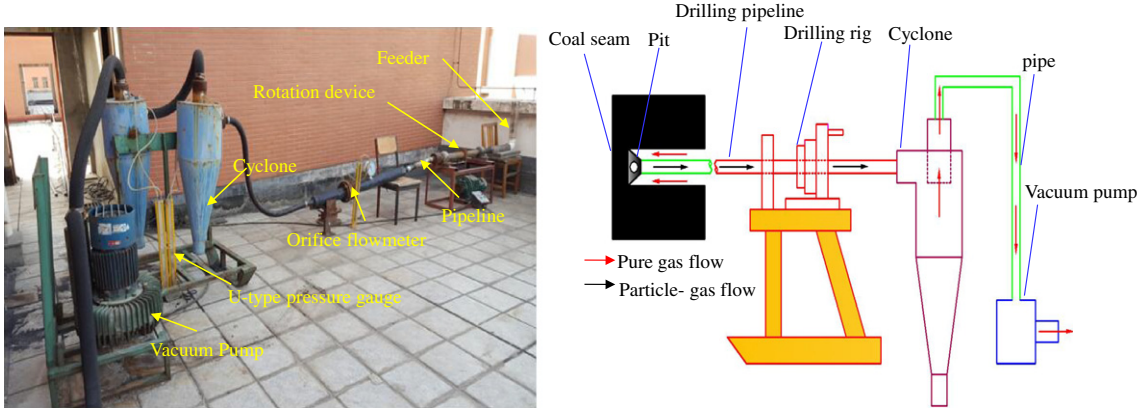
where i, j, and k are the three directions in a Cartesian coordinate system; D_{ij}, P_{ij}, ϕ_{ij}, and ϵ_{ij} represent the diffusion term, stress generation term, dispersion term, and turbulence viscosity, respectively, and u_i', u_j' and u_k' are the velocity fluctuations, respectively.

2.2. Cyclone

The infield cyclone working conditions in the Xin'an coal mine, which is located in Xin'an County, Luoyang, Henan Province, were examined in this study. The Xin'an coal mine is classified as a coal and gas outburst coal mine. The main production coal seam was 2_1 (2^1 in Page 6 is incorrect and should be 2_1. The main production coal seam, i.e. the main mining coal seam, which means the coal seam are available for mining and is under mining now. 2^1 is the coal seam name. The naming of coal seam is based on the specification released by the Coalfield Geology Bureau of Henan Province, China. The coal-bearing stratum is divided into 9 groups, i.e. 1 to 9. Each group contains several stratums. Group 2 contains 3 stratums, i.e. 1, 2 and 3 from up to down. Xin'an coal seam belongs to the group 2 and stratum 1. So the main production coal seam is named as 2_1), with an incline angle of 6° to 9°, and an average angle of 6°. The coal quality was tectonic meager-lean coal, with a Protodyakonov coefficient of between 0.15 and 0.3. The coal seam thickness was approximately 0 to 9.5 m, with an average thickness of 3.79 m.

The technology scheme of the sampling method based on negative pneumatic conveying to determine the coal bed methane content, is shown in Fig. 2. The system of the sampling method based on the negative pneumatic conveying (Fig. 2(a)) consisted of a vacuum pump, cyclone, equivalent static drilling pipe, dynamic drilling pipe, and feeder. The working principle was that the pure gas was exhausted into the borehole bottom, and then mixed with the coal particles which were falling down from the coal walls into the gas-solid flow. Next, the flow entered into the drilling pipe through the fluid hole. The gas-solid flow travelled through the drilling pipe to the cyclone, and collected there. The gas-solid flow was driven by a vacuum pump, as illustrated in Fig. 2(b).

During this method process, the vacuum pump was selected as the power source, and the pressure ranged from −50 to 40 kPa. A rectangle tangential cyclone, with a wall thickness of 3 mm and a maximum gas flow capacity of 9 m^3/min, was used as the sampling collector. There were two pressure test holes at a 180° distribution in both the inlet and outlet. The pressure was measured using a "U" type pressure gauge, and the two inlets were connected with the two pressure test holes by a hosepipe. The equivalent static drilling pipe was a PVC pipe, with a specification of ø50 mm × 4000 mm. The gas-solid flowed into the dynamic drilling pipe through the fluid holes. The feeder was simulated using an organic glass tube with a diameter of 100 mm. The coal



(a) Experimental setup for sampling method based on negative pressure pneumatic conveying

(b) Scheme diagram of sampling method based on negative pressure pneumatic conveying

Fig. 2. Cyclone working condition.

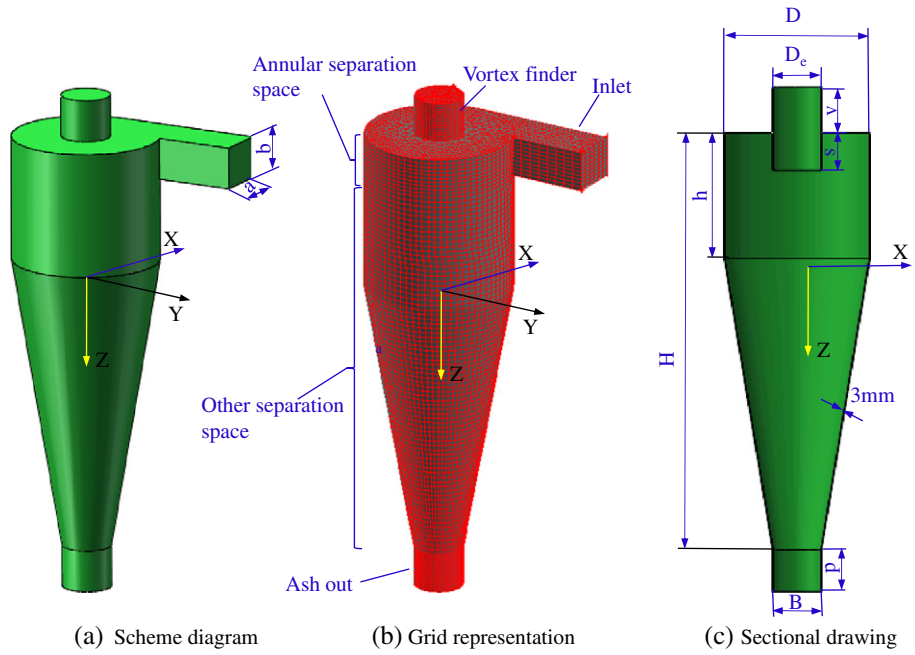


Fig. 3. Scheme diagram and grid of cyclone current simulation.

particles entered into the tube, and moved forward with a specified velocity.

The gas flow rate was measured by using a combination of a"U"type pressure gauge, and an orifice-flowmeter. The coal particles used were anthracite coal. The particles' densities were approximately 1400 kg/m^3, and the mean particle diameter was 2 mm. The tests were carried out at an atmospheric pressure, ambient temperature, and relative humidity of 100.1 kPa, 301.3 K, and 86%, respectively. The inlet solid ratios were set at 0.72, 2.16, 4.32, 6.48, and 8.64 kg/kg, with a gas velocity of 6 m/s, and a coal particle velocity equaling 16 m/s.

The cyclone was constructed by SOLIDWORKS Premium 2010 (Dassault Systèmes SOLIDWORKS Corp, MA, USA), as shown in Fig. 3, and the dimensions are shown in Table 1. A block division was adopted to mesh the computational domain. The whole computational domain was divided into five parts as follows: inlet; annular separate space; vortex finder; ash out; and other separation space. All of these were meshed into tetrahedron mesh using Gambit (Gambit2.4.6, PA, USA) as shown in Fig. 3(b). Fig. 3(c) shows the sectional drawing from the XOZ view. Then, three grid domains were tested containing 68,706, 105,592 and 172,034 cells, respectively. The pressure drop was selected for the purpose of validating this study's results, and the difference in the three simulations were determined to be less than 5%, as shown in Table 2.

Table 1
The cyclone geometry for current simulation (m).

D	a	b	B	H	h	D_e	S	V	p
0.3	0.1	0.1	0.1	1.1	0.4	0.1	0.1	0.1	0.1

Table 2
The details for the grid independence study.

Cell number	Pressure drop (Pa)	%difference[a]
68,706	221	4.5%
105,592	231	
172,034	228	

[a] The difference between the coarsest grid and finest grid.

2.3. Gas-solid simulation

2.3.1. Modeling and meshing

In the gas phase calculation, a PISO (Pressure-Implicit with Splitting of Operators) algorithm was selected for the pressure-velocity coupling. The discretization of the momentum and pressure were QUICK (Quadratic Upstream Interpolation for Convective Kinetics), and PRESTO! (Pressure Staggered Option), respectively. A Second Order Upwind scheme was selected for the turbulent kinetic energy, turbulent dissipation rate, and Reynolds stress, respectively [25]. The particle phase parameter included four parts: the particle physical property, wall physical property, particle-particle interaction coefficient, and particle-wall coefficient. All of the parameters were selected based on the empirical, as shown in Table 3. The particle physical property included, a particle diameter of 2 mm, and a particle density of 1400 kg/m^3. The shear modulus was 1.4×10^9 Pa, and the Poisson's ratio was 0.201. The wall physical property included: a wall density of 7400 kg/m^3; shear modulus 8.24×10^{10} Pa; and Poisson's ratio of 0.25. The particle-particle interaction coefficient included: a particle-particle restitution coefficient of 0.5; particle-particle static friction coefficient of 0.6 and particle-particle dynamic friction coefficient of 0.05. The particle-wall interaction coefficient included: particle-wall restitution coefficient (0.5), particle-wall static friction coefficient (0.4) and particle-wall dynamic friction coefficient of 0.05.

Table 3
Particle and wall material parameters [28].

Properties	Unit	Value
Coal density	kg·m^{-3}	1400
Coal particle diameter	mm	2
Coal shear modulus	Pa	1.4e9
Coal Poisson's ratio	–	0.201
Steel density	kg·m^{-3}	7400
Steel shear modulus	Pa	8.24e10
Steel Poisson's ratio	–	0.25
Coal-coal restitution coefficient	–	0.5
Coal-coal static friction coefficient	–	0.6
Coal-coal rolling friction coefficient	–	0.05
Coal-steel restitution coefficient	–	0.5
Coal-steel static friction coefficient	–	0.4
Coal-steel rolling friction coefficient	–	0.05

During the FLUENT-EDEM coupling simulation, the gas phase first reached a steady level, and then the particle phase flowed in. The gas phase reached a convergence in a single phase time-step. The particles up-dated the motion in a single particle time-step by the gas phase data in the cell. In the next new single phase time-step, the gas phase updated the gas phase in the computational domain to a convergence point. The gas and particle phases were calculated to the steady level, as mentioned above.

An inlet velocity boundary was selected at the cyclone's inlet and was normal to the inlet. The study included two parts, i.e. one was the different solid-gas ratios under the same gas velocity/particle velocity ratio. The other part was the different gas velocity/particle velocity ratios under the same solid gas ratio. For the first part, the gas velocity was set as 6 m/s, while for the second part, the gas velocities were set as 10 m/s, 12 m/s and 14 m/s in the second part, respectively. The outlet boundary was set as the outflow, and the other boundaries were set as a no slip boundary condition. The gas flow time-step was 1e-04 s. Then, the dynamic particle production was selected. The particle velocity was set 16 m/s, and was normal to the inlet.

2.3.2. Model validation

In order to validate the RSM model, the pure gas flow in cyclone was investigated. An inlet velocity boundary was selected at the cyclone's inlet and was normal to the inlet. The outlet boundary was set as the outflow, and the other boundaries were set as a no slip boundary condition. The gas flow time-step was 1e-04 s and all the simulations run 2 s. Also the pressure-velocity coupling algorithm was set PISO (Pressure-Implicit with Splitting of Operators). The discretization of the momentum and pressure were QUICK (Quadratic Upstream Interpolation for Convective Kinetics) and PRESTO! (Pressure Staggered Option), respectively. All of the turbulent kinetic energy, turbulent dissipation rate, and Reynolds stress were set Second Order Upwind scheme, respectively.2.3.3 Simulation

In the pure gas flow study, the inlet velocity were 4 m/s, 6 m/s, 8 m/s,10 m/s, 12 m/s, respectively. The cyclone pressure drop was investigated. Since the pressure drop is the main parameter to value the cyclone performance, the pressure drop was analyzed for the each simulation.

In this study, eight cases were carried out, as shown in Table 4. Case 1 to Case 5 are examined to study the working conditions with different solid gas ratios under the same gas velocity/particle velocity ratio. Case 6 to Case 8 were carried out to study the working conditions with different gas velocity/particle velocity ratios under the same solid gas ratio. All of the cases run for 2 s.

The static pressure distribution reflected the transformation between the static and dynamic pressures. Since the gas phase evolutions were different, the static pressures were analyzed for the each of the eight cases.

The tangential, axial, and radial velocities were the gas-flow's three components, and were affected by the solid gas ratio. Therefore, the tangential, axial, and radial velocities were analyzed for each of the eight cases.

Table 4
Cases settings.

	Case	Gas velocity (m/s)	Gas velocity (m/s)	Particle generation rate (kg/s)	Solid gas ratio (kg/kg)[a]
Different solid gas ratios with same gas velocity/particle velocity ratio	1	6	16	0.05	0.72
	2	6	16	0.15	2.16
	3	6	16	0.30	4.32
	4	6	16	0.45	6.48
	5	6	16	0.60	8.64
Different gas velocity/particle velocity ratios with same solid gas ratio	6	10	16	0.107	0.89
	7	12	16	0.128	0.89
	8	14	16	0.150	0.89

[a] The solid gas ratio corresponding to the particle generation rate.

The particle flow pattern was determined to be related to the particle residence time, as well as the particle separation. The particle residence time and separation process increased when the particle flow pattern was not clear. However, when the particle flow pattern became clear, the particle residence time and separation process decreased. The particle flow patterns were analyzed for each of the eight cases.

The interaction of the gas-particle, particle-particle, and particle-wall forces were found to be the three forces which existed in the gas-solid flow. The study of the formation and evolution for these three forces will assist in an improved comprehensive understanding of the particle flow pattern, along with the determination of the main reasons for the inducement of particle breakage and wall attrition. The interaction of the gas-particle, particle-particle and particle-wall forces were analyzed for the Case 1 to Case 5.

3. Results

3.1. Simulation results

3.1.1. Model validation

Pressure drop is main parameters for cyclones and is used to validate in this study. Fig. 4 showed the pressure drop of RSM simulated results under different inlet velocities, which were compared with reference pressure drop empirical formulas provided by Shepherd & Lapple [41], Dirgo [42] and Coker [43]. The RSM simulated pressure drop were 321 Pa, 585 Pa, 916 Pa, 1319 Pa and 1788 Pa for 6 m/s, 8 m/s, 10 m/s, 12 m/s, 14 m/s inlet gas velocity, respectively. The RSM simulated results were close to the Shepherd & Lapple [41], while a lager difference existed among the Dirgo [42] and Coker [43]. As for a certain cyclone geometry, the cyclone local frictional coefficient was almost a constant. So the pressure drop change tendency was consistent. The results showed that the RSM simulated results qualitatively agreed with the trends reported in [41–43]. The compared results also showed that the RSM was validated to describe the gas flow in cyclone.

3.2. Gas-solid flow characteristic with same gas velocity/particle velocity ratio under different solid gas ratios

3.2.1. Static pressure

Fig. 5 shows the static pressure distribution under the different solid gas ratios. The static pressure distribution was mainly divided into four areas: the negative pressure area, static pressure strand, high pressure area, and low static pressure area. In Case 1 (solid gas ratio = 0.72 kg/kg), the negative pressure area existed in the vortex finder. The static pressure strand appeared with a tail wag structure, from the cyclone top, to the ash out. The high pressure area existed the entire separation space near the wall, and the area was wider in the cylindrical separation space than in the conical separation space. In Case 2 (solid gas ratio = 2.16 kg/kg), the negative pressure area was not changed.

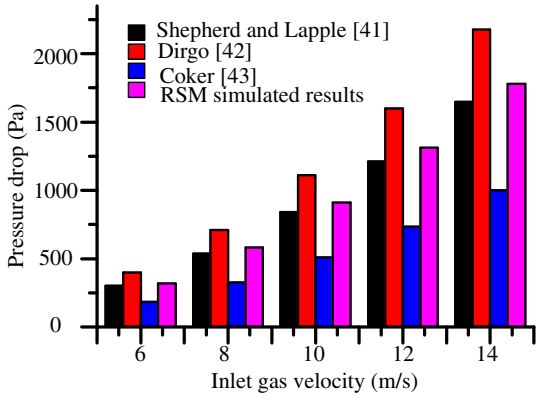


Fig. 4. The pressure drop of RSM compared with reference data from the literature.

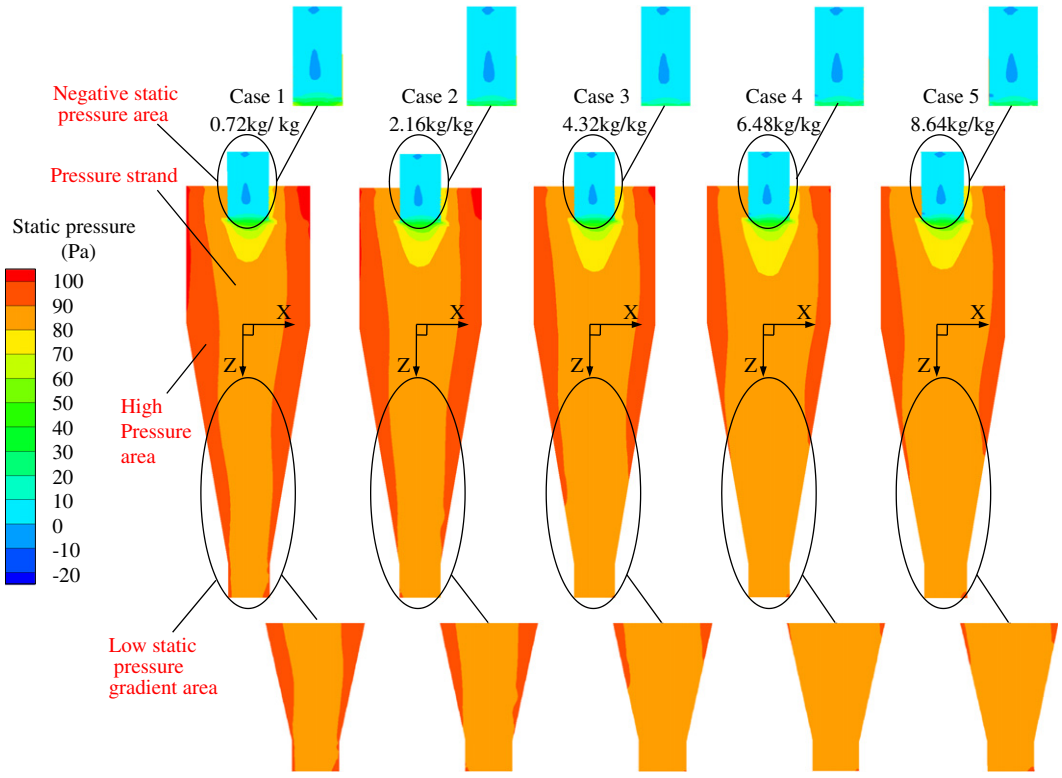


Fig. 5. Static pressure distributions at the central section vertical to the cyclone inlet under different solid gas ratios.

As the pressure strand width became wider, the high pressure area disappeared into the ash out, and the low static pressure gradient area became larger. In Case 3 (solid gas ratio = 4.32 kg/kg), the pressure strand width became further widened, the high pressure area moved forward, and the low static pressure gradient area became further enlarged. In Case 4 (solid gas ratio = 6.48 kg/kg), the pressure strand width became further widened, the high pressure area moved forward, and the low static pressure gradient area became further enlarged. In Case 5 (solid

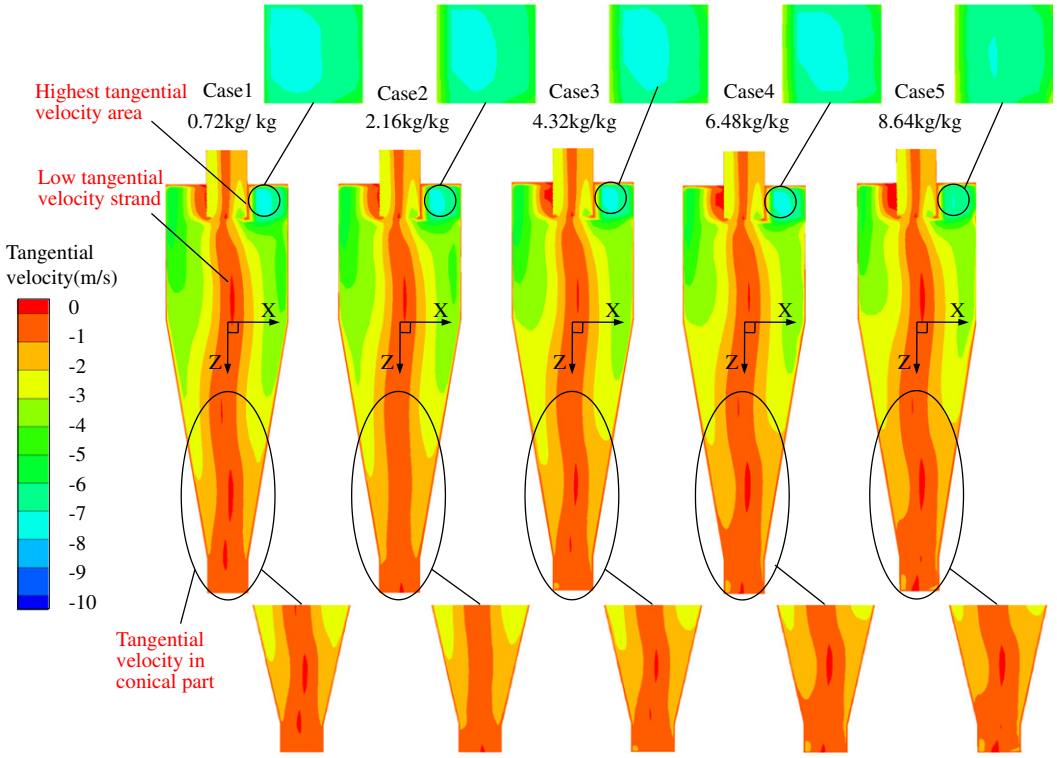


Fig. 6. Tangential velocity distributions at the central section vertical to the cyclone inlet under different solid gas ratios.

gas ratio = 8.64 kg/kg), the pressure strand width, high pressure area, and low static pressure gradient area all remained steady.

3.2.2. Tangential velocity

Fig. 6 shows the tangential velocity distribution under the different solid gas ratios. Included are the highest and lowest tangential velocity areas. The highest tangential velocity area appeared to be to the right of the inlet part, and the area was smaller than that of the inlet. The highest tangential velocity area was found in Case 1. The low tangential velocity area appeared with a tail wag structure, from the cyclone's outlet area to the ash out area. In Case 2, the highest tangential velocity area became lessened, and the low tangential velocity area width became wider, similar to Case 3. In Case 4, the widths of the low tangential velocity and conical separation space areas became wider, and the solid gas ratio was less than 6.42 kg/kg. In Case 5, the tangential gradient in the conical separation space further decreased, and the highest tangential area almost disappeared.

3.2.3. Axial velocity

Fig. 7 illustrates the axial velocity distribution under the different solid gas ratios. The axial velocity distribution mainly included four areas: the highest axial velocity, low axial velocity, high axial velocity strand, and low axial gradient areas. The highest axial velocity area appeared in the vortex finder. The low axial velocity area appeared near the separation space wall. The high axial velocity strand appeared as a tail wag structure in the inner part of the separation space. The low axial gradient area appeared in the conical separation space. In Case 1, the highest axial velocity area appeared in the vortex finder. The low axial velocity area appeared near the cylindrical separation space wall, and the area was very small. In Case 2, the highest axial velocity area remained steady, the tag of the high axial velocity strand moved upward, and the low axial gradient area became larger. In Case 3, the highest axial velocity still remained steady, the axial velocity strand moved further upward, and the low axial velocity area became larger in the conical separation space. In Case 4, the high axial velocity strand moved upward, and the low axial velocity area increased slightly. In Case 5, the high axial velocity strand moved farther downward than in Case 4, and the low axial velocity area increased somewhat.

3.2.4. Radial velocity

Fig. 8 demonstrates the radial velocity distribution under the different solid gas ratios. From Fig. 8, it can be seen that the radial velocity distribution was symmetrical, and the symmetry axis was almost a straight line, which was from the apex center to the vortex finder center. The axial velocity was low, with a range from −2.0 m to 0.4 m/s. Two of the highest radial velocity areas appeared near the vortex finder. However, these areas were not equal. In Case1, the radial velocity was low in the conical separation space. In Case 2, the radial velocity in the conical separation space increased. In Case 3, the radial velocity in the conical separation space become larger than that in Case 2, and the symmetry was apparent. The radial velocity remained steady in Cases 4 and 5

3.2.5. Particle flow

Fig. 9 shows the particle flow pattern in the cyclone under the different inlet solid gas ratios. The particle strand became clear, and remained steady. In Case 1, the particle residence time and separation process increased when the particle flow pattern was not clear. In Case 2, the particle flow pattern formed, and the particle flow tendency became consistent. However, in Cases 3, 4, and 5, the particle flow pattern forms were clearer, and remained steady.

The particles flowed into the cyclone and turned at some points, as shown by the first and second turning points in Case 5 (Fig. 9). The two turning points changed with the particle flow pattern. The descending distance was defined as the distance between the inlet bottom line and the first turning and second turning points, which were L_1, and L_2, respectively, and the descending distance under the different solid gas ratios, as shown in Table 5.

A top ash ring appeared at the annular separation space in all of the cases, and became stronger between Case 1 to Case 3, at which point the top ash ring then remained steady.

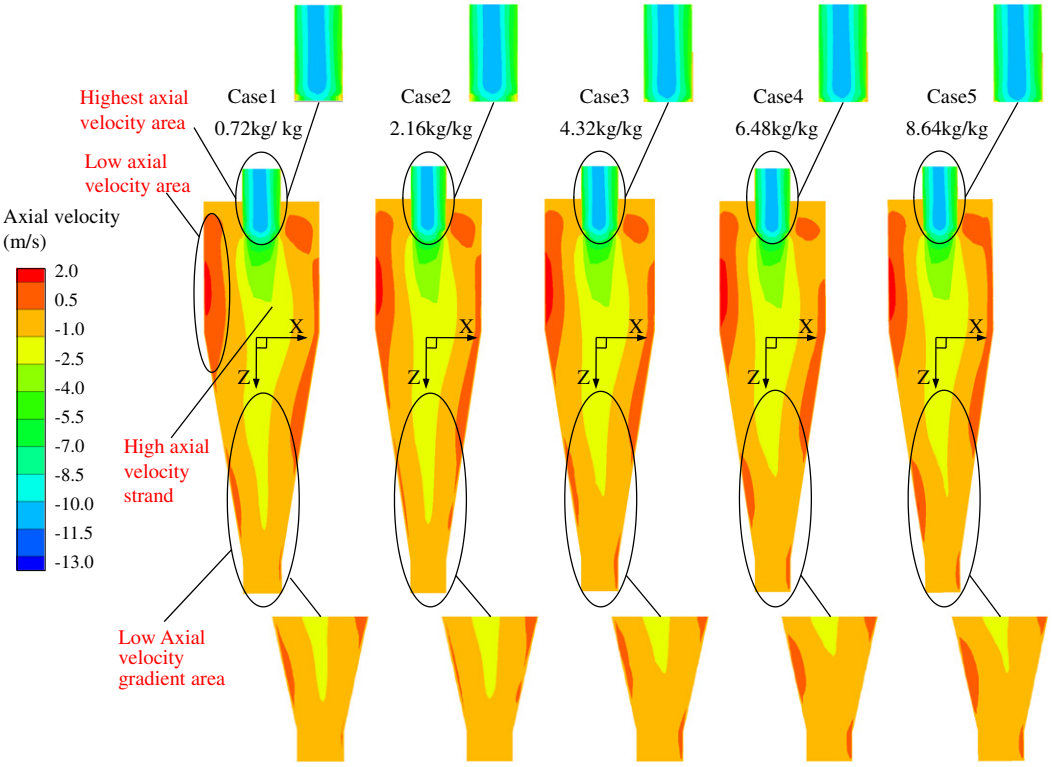


Fig. 7. Axial velocity distributions at the central section vertical to the cyclone inlet under different solid gas ratios.

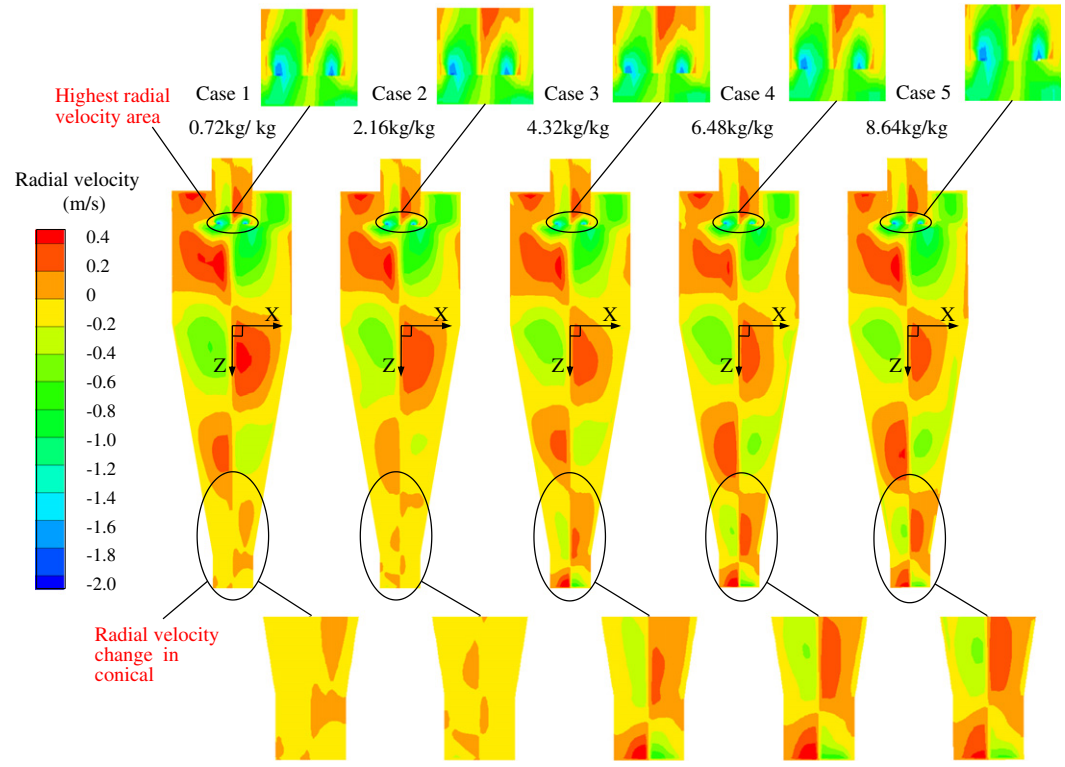


Fig. 8. Radial velocity distributions at the central section vertical to the cyclone inlet under different solid gas ratios.

3.2.6. Gas-solid flow interaction

Fig. 10 shows the gas-solid coupling force under the different solid gas ratios. The gas-solid coupling force first increased, and then remained steady under the same solid gas ratio. The increased times lasted 1.2, 1.0, 0.8, 0.75 and 0.73 s when the solid gas ratios were 0.72, 2.16, 4.32, 6.48 and 8.64 kg/kg, respectively. The corresponding gas-solid coupling forces at a steady state were 5000, 10,000, 23,000, 32,000, and 40,000 mg, respectively.

Fig. 11 shows the particle-particle and particle-wall interactions under the different solid gas ratios. The contact numbers of the particle-particle and particle-wall first increased, and then remained steady under the same solid gas ratio, as shown in Fig. 11(a) and 11(b). The contact numbers of the particle-particle were 10,250, 500, 1250 and 2250 when the steady level was reached, and when the solid gas ratios were 0.72, 2.16, 4.32, 6.48,and 8.64 kg/kg, respectively. The contact numbers of the particle-wall were 50, 100, 200, 300, and 450, respectively.

The forces of the particle-particle and particle-wall interactions first increased, and then remained steady under the same solid gas ratio, and with the large fluctuation, as shown in Fig. 11(c) and (d). The increasing times for the particle-particle and particle-wall interactions were 1.2, 1.0, 0.8, 0.75 and 0.73 s when the solid gas ratios were 0.72, 2.16, 4.32, 6.48 and 8.64 kg/kg, respectively. The forces of the particle-particle interactions were 0.25×10^5 mg,1.25×10^5 mg,2.1×10^5 mg,3.15×10^5 mg,5.5×10^5 mg, and the particle-walls were 0.25×10^6 mg,0.75×10^6 mg,1.25×10^6 mg,2×10^6 mg, and 2.30×10^6 mg, respectively.

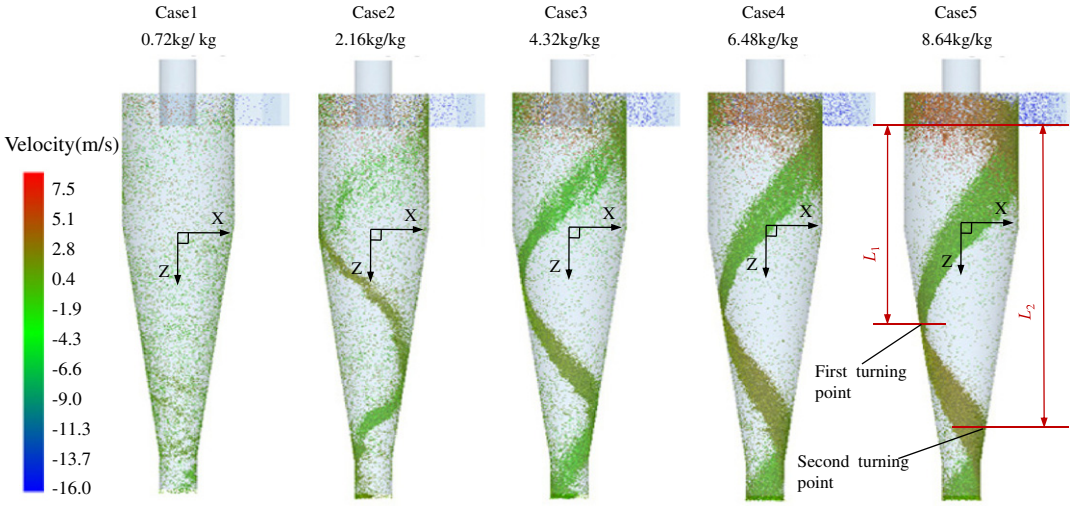


Fig. 9. Particle flow pattern in cyclone under different solid gas ratios(at $t = 2$ s).

Table 5
The descending distance change under different solid gas ratio.

Case	Solid gas ratio (kg/kg)	L_1(m)	L_2(m)
1	0.72	–	–
2	2.16	0.35	0.75
3	4.32	0.51	0.83
4	6.48	0.54	0.9
5	8.64	0.60	0.91

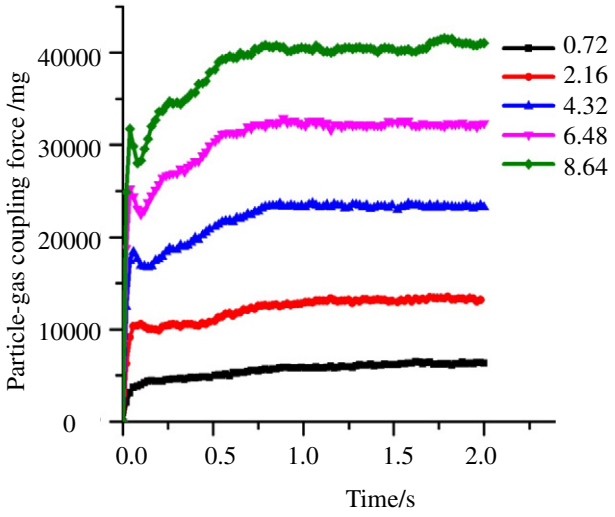


Fig. 10. Particle–gas coupling force under different solid-gas ratios.

3.3. Gas-solid flow characteristic with the different gas velocity/particle velocity ratios under the same solid gas ratio

3.3.1. Static pressure

Fig. 12 shows the static pressure distribution of the working condition with different gas/particle velocity ratios under the same solid gas ratio in the cyclone. The pressures include negative pressure area, static pressure strand and high pressure area with static pressure distribution. In Case 6, negative pressure area exists in the vortex finder, which distributes in strip shape. The static pressure strand forms in the center position with swing tail distribution. The high static pressure area exists in conical separation space. In Case 7, the static pressure in the static pressure strand increases. The shape of the negative pressure area forms sheet shape, and the negative pressure value and the high static pressure value in conical part increases. In Case 8, the slice area of the negative pressure area and the negative pressure value increase as well. The high static pressure area in the conical separation space increases continuously. There is a significant difference in the pressure of the conical separation space.

3.3.2. Tangential velocity

Fig. 13 illustrates the tangential velocity distribution of the working condition with different gas/particle velocity ratios under the same solid gas ratio in the cyclone. The tangential velocity distribution in cyclone has the highest tangential velocity area and the low tangential velocity area. In Case 6, the highest tangential velocity area exists vertical to the entrance and the area was less than the entrance section. The low tangential velocity strand area is in the vortex finder and separation space. The low tangential velocity strand area in separation space is shown as “swing tail”. In Case 7, the highest tangential velocity area

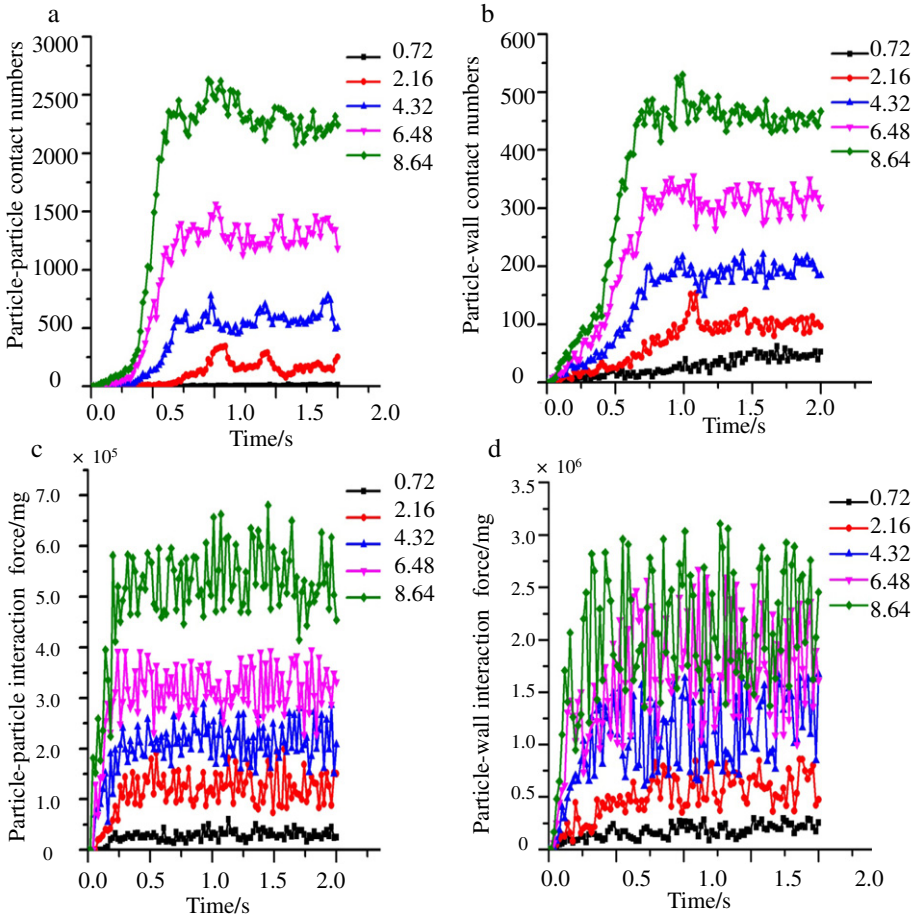


Fig. 11. Particle-particle interaction and particle-wall interaction under different solid gas ratios.

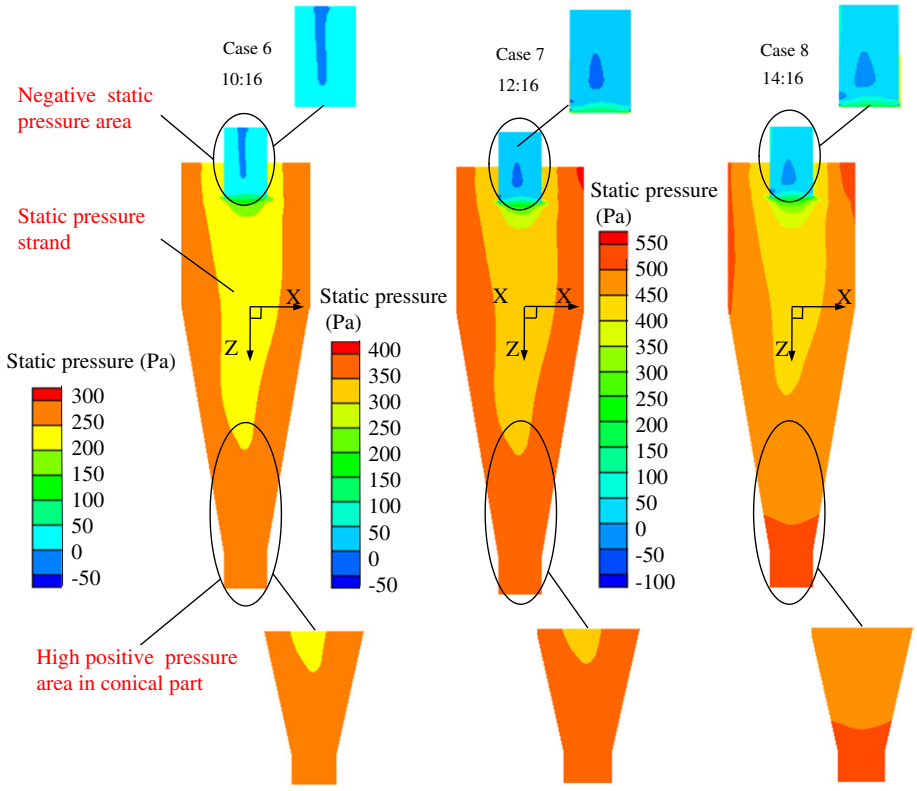


Fig. 12. Static pressure distributions at the central section vertical to the cyclone inlet under different gas velocity/particle velocity ratios at same solid gas ratio ($t = 2$ s).

increases. The low tangential velocity strand becomes narrower in the separation space, also for the tangential velocity in conical part. In Case 8 the highest tangential velocity area increases, compared with Case 7. At the same time, the low tangential velocity strand area becomes narrower in the separation space and the tangential velocity in conical part goes down continuously.

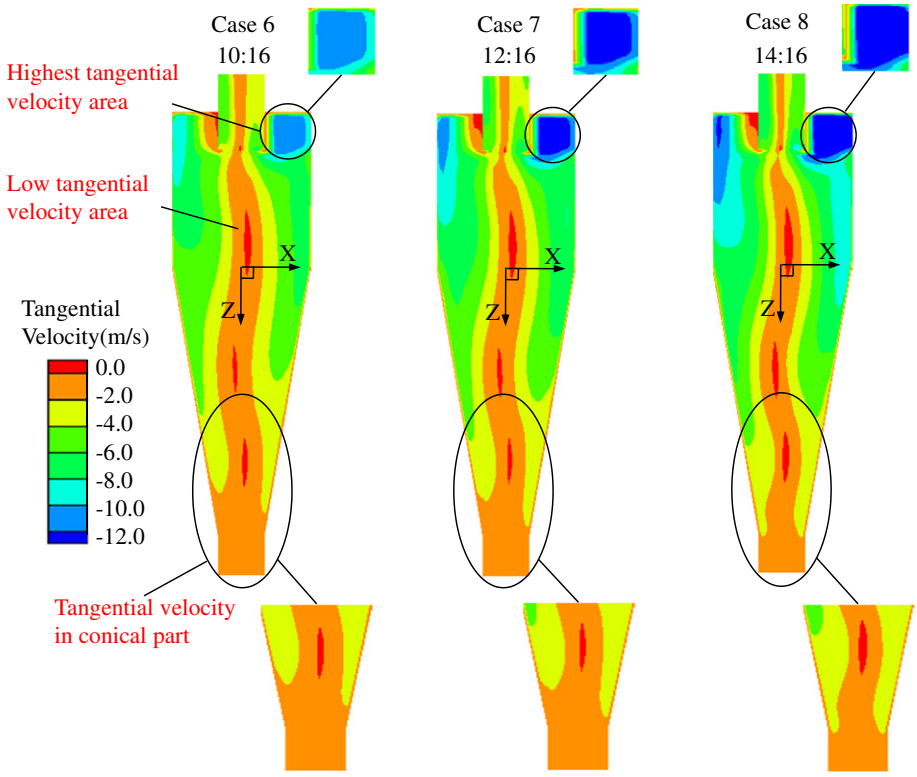


Fig. 13. Tangential velocity distributions at the central section vertical to the cyclone inlet under different gas velocity/particle velocity ratios at same solid gas ratio ($t = 2$ s).

3.3.3. Axial velocity

Fig. 14 presents the axial velocity distribution of the working condition with different gas/particle velocity ratios under the same solid gas ratio in the cyclone. The axial velocity distribution mainly includes two areas, i.e. the highest axial velocity area and the high axial velocity area. In Case 6, the highest axial velocity area distribution is in vortex finder; and the high axial velocity strip distribution is in the separation space. In Case 7, the highest axial velocity area becomes larger; the strip tail of high axial velocity moves down and becomes wider. In Case 8, the highest axial velocity area continues to increase and the strip tail of high axial velocity moves down continuously.

3.3.4. Radial velocity

Fig. 15 demonstrates the radial velocity distribution of the working condition with different gas/particle velocity ratios under the same solid gas ratio in the cyclone. It distributes in axial symmetry, and the symmetrical axis is the line from the center of the vortex finder to the center of the ash out. In Case 6, the two highest radial velocity areas appear in the bottom of the vortex finder. In Case 7, the highest radial velocity area becomes larger and the radial velocity in the conical separation space increases. From Case 7 to Case 9, the highest radial velocity area enlarges furtherly and the radial velocity in the conical separation space increases continuously.

3.3.5. Particle flow pattern

Fig. 16 presents the particle flow pattern of the working condition with different gas/particle velocity ratios under the same solid gas ratio in the cyclone. The particle flow pattern in the cyclone distributes with strand distribution and dispersion distribution. In Case 6, particle distribution in the cylindrical separation space scatters. But below the interface between the cylindrical separation space and conical separation space (see 1# in Fig. 16), forms a fuzzy particle strand. The particle flow pattern in the conical separation space distributes as strand. In Case 8, particle distribution in the cylindrical separation space is still scattered. However, above the interface between the cylindrical separation space and conical separation space forms a fuzzy particle strand (see 2# in Fig. 16). And the particle distribution in the cylindrical separation space distributes as strip distribution. In Case 8, particle distribution in the cylindrical separation space still is scatted. But a fuzzy particle strand forms (see 3# in Fig. 16).

3.4. Experimental results

A series of parameters about pressure drop were selected and validated by the experiment. Table 6 shows the simulated pressure drop along with the experimental drop under the different inlet solid ratios.

It can be seen from the Table 6, that the experimental text results of the pressure drop were 125, 90, 85, 80, and 80 Pa when the solid gas ratios were 0.72, 2.16, 4.32, 6.48, and 8.64, respectively. Also, the simulated results were 102, 98, 92, 90, and 91 Pa. Although the simulated results were higher than that of the experiment, the change trend was in high agreement with the experimental results. The difference may have been caused by the measurement method, in which the experimental results were always lower than the real values using this method [44]. Therefore, the result differences were determined to be acceptable.

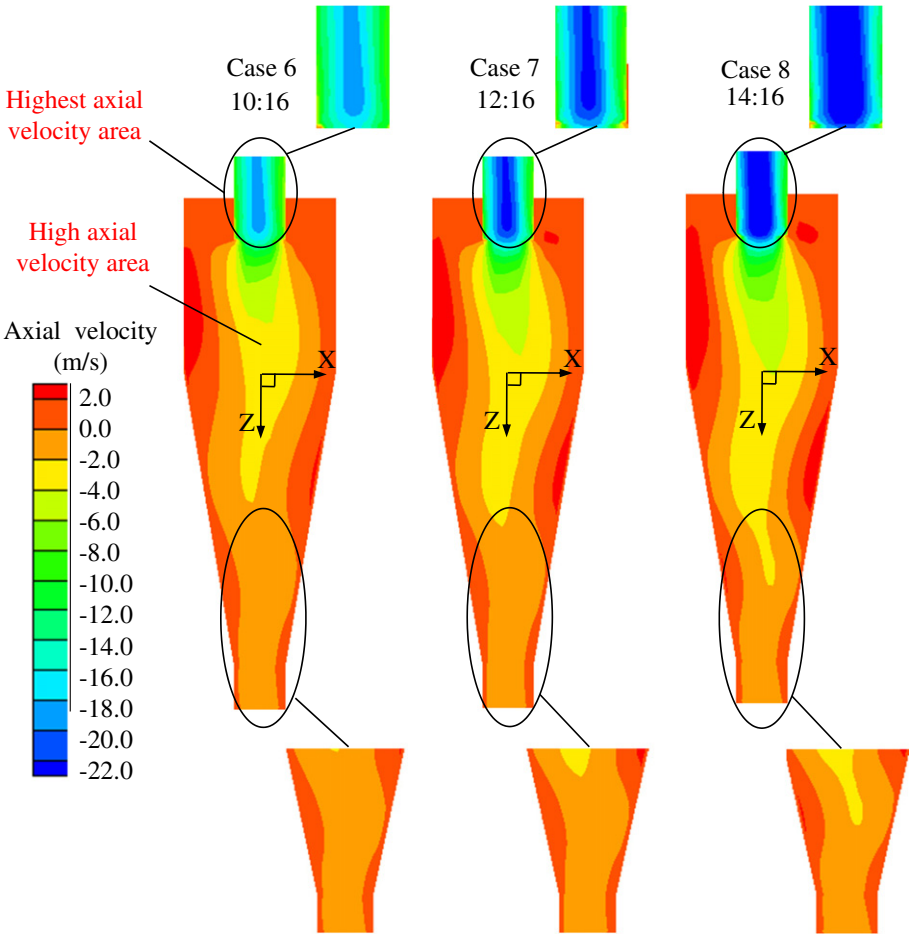


Fig. 14. Axial velocity distributions at the central section vertical to the cyclone inlet under different gas velocity/particle velocity ratios at same solid gas ratio ($t = 2$ s).

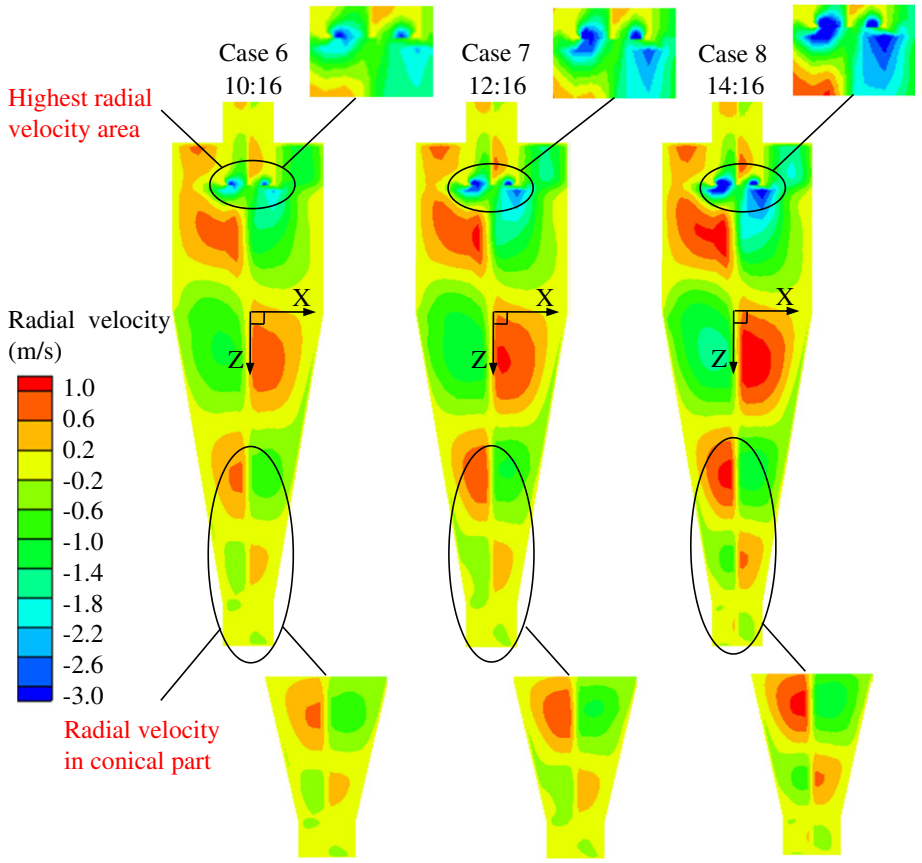


Fig. 15. Radial velocity distributions at the central section vertical to the cyclone inlet under different gas velocity/particle velocity ratios at same solid gas ratio ($t = 2$ s).

4. Discussion

It was found that the cross section between the pneumatic conveying pipe and cyclone inlet were not consistent. The particle velocity was higher than that of the gas, which easily led to particle breakage and wall attrition. The particle breakage resulted in a lower particle grade and wall attrition, which accelerated the scrapping of the cyclones, and increased the cost. As the gas-solid flowed into the cyclone, the gas turned and swirled, moving downward to the bottom of the cyclone. The particles were moved forward to the wall due to the centrifugal force and resistance. The particles were no longer inert, and were moved downward by the gravity. In this study, the gas-solid flow in a

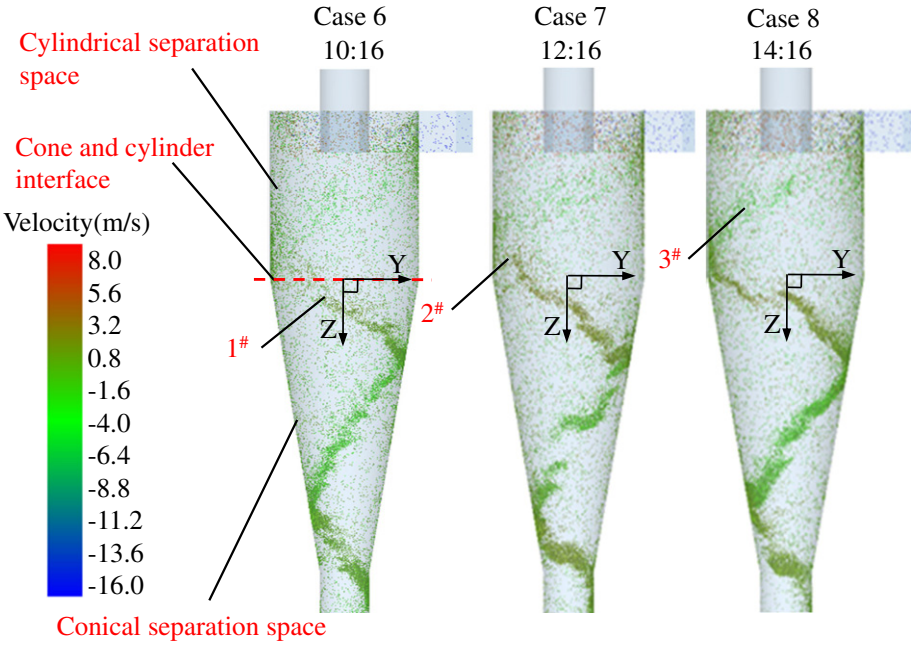


Fig. 16. Particle flow pattern in cyclone under different gas velocity/particle velocity ratios at same solid gas ratio ($t = 2$ s).

Table 6
Comparison of the simulated and experimental pressure drop under different solid gas ratios.

Case	Solid gas ratio(kg/kg)	Experimental result (Pa)	Simulated result (Pa)
1	0.72	125	102
2	2.16	90	98
3	4.32	85	92
4	6.48	80	90
5	8.64	80	91

cyclone was investigated using FLUENT-EDEM. The results revealed the underlying causes of the gas-solid flow in a cyclone.

The results showed that the existence of particles had a major effect on the gas flow of the cyclone in the inlet and conical separation parts, as shown in Figs. 5 to 8. The static pressure distribution reflected the static pressure, as well as the dynamic pressure transformation. When the gas velocity was higher than the particle velocity, the static pressure transformed into dynamic pressure for a strong gas turbulence phase, and a negative pressure area formed in the separation space [11,45,46].When the particle velocity was higher than the gas velocity, a strong gas turbulence phase appeared only in the vortex finder, and a negative pressure appeared, as shown in Fig. 5. The tangential velocity (Fig. 6), axial velocity (Fig. 7), and radial velocity (Fig. 8) changed little, and were mainly affected by the solid gas ratios in the conical separation space and inlet at the same gas velocity/particle velocity ratio. The tangential velocity, axial velocity and radial velocity increase with the increasing of the gas velocity/particle velocity ratio under the same solid gas ratio. The strong turbulence only occurs in the vertex finder, so the negative pressure exists in this part. The particle mass (i.e. the particle number) decreases with the gas velocity/particle velocity ratio increasing under the same solid gas ratio. The direction of force acting on phase by particle is upward and the particle existing prevented gas from flowing downward [47]. Hence, the less particle number, the weaker acting on the phase flow by particle and the gas flow in the cyclone had strong tendency flowing like pure gas. So the tangential velocity (Fig. 13), axial velocity (Fig. 14) and radial velocity (Fig. 15) increase.

The particle flow pattern formed and remained steady when the gas velocity was lower than the particle velocity with same gas velocity/particle velocity ratio under the different solid gas ratios, as shown in Fig. 9. Turbulence, diffusion, and agglomeration phenomena were evident in the gas-solid flow within the cyclone. When the solid gas ratio was low (as in Case 1), the particle turbulence and diffusion played a dominant role, and the agglomeration was weak. This led to particle dispersion, and the particle flow pattern was not formed. From Case 1 to Case 5, the agglomeration played a dominant role. When the gas velocity was lower, the centrifugal force acting on the particles was less than the gravitational force, and the particle strand flowed downward. The particle flow pattern formed and remained steady with the increases in the solid gas ratio. Fig. 16 shows the particle flow pattern at the same solid gas ratio under different gas velocity/particle velocity ratios. The particle strand forms different start point under same solid gas ratio at different gas velocity/particle velocity ratio, i.e. $1^{\#}$ in Case 6, $2^{\#}$ in Case 7 and $3^{\#}$ in Case 8. At the same solid gas raito, the particle number decreases with the increasing of gas velocity, leads to the particle agglomeration effect weaker. For the particle dispersion stronger, the particle distribution in the upper part is scattered. The particle flow follows tendency and become stronger with the increasing of gas velocity. So the start point of particle strand increases with the increasing of gas velocity/particle velocity ratio. When the DPM model was adopted to describe the particle (diameters larger than 0.1 mm) flow in the cyclone, the particles remained rotating horizontally. In regards to the particles flowing into the conical separation space, the gas-solid flow radius became shorter, the gas velocity became enlarged, the particle velocity changed slightly, and the particles obtained a higher centrifugal force [48]. However, when the FLUENT-EDEM coupling simulation was adopted, all of the particles flowed downward and out, as shown in Fig. 9. Therefore, the effects of particle-particle collision should be considered in order to describe the larger particles and high solid gas ratio. The particle strand's descending distance became longer with the increases of the solid gas ratio, which suggested that the gravitational force was the main reason for the particle strand's descent when the particle velocity was higher than the gas. Then, the increment became lessened, which suggested that the particle flow pattern was only minimally affected by increased solid gas ratio. The increment of the particle strand's descending distance could be reduced by the particle residence time and accelerated by the separation process. When the particle velocity was higher than the gas velocity, an ash top ring appeared and became stronger with the increases in the solid gas ratio. The drag and centrifugal forces in a radial direction acted on the particles in the annular separation space, and the gravitational and drag forces were induced by the axial velocity in a vertical direction [48]. When the particle velocity was lower than gas velocity, the top ash ring became weaker [47]. When the particle velocity was higher than the gas, the gas phase turbulence in the annular separation space was weak. The particles flowed into the cyclone with a high centrifugal force, and the centrifugal force played a main role. However, the centripetal force was not large enough to cause the particles move downward along the vortex finder wall to the vortex finder bottom, and the centrifugal force and gravity caused the particles to move with the strong turbulence into the annular separation space.

When the particle velocity was higher than the gas velocity, the particle-wall interaction force was the largest. The drag force played a major role in the gas-solid coupling force [47], since the drag force had a positive relationship with the particle projected area. The higher the solid gas ratio became, the larger the particle projected area became, which led to increases in the gas-solid coupling force. The particle-particle contact numbers and the particle-wall contact numbers are shown in Fig. 11(a) and 11(b), respectively. The particle residence in the cyclone became nonlinear with the increases in the solid gas ratio, which led to the particle-particle contact number increasing. For a given inlet structure, the particles flowed uniformly into the cyclone. The particle turbulence and diffusion became weaker, and the agglomeration phenomena became stronger, while the particle flow pattern changed only slightly, and increased in thickness. Therefore, the particle-wall contact numbers increased somewhat. When the particle velocity was higher than the gas velocity, the particle-wall interaction force became larger than the particle-particle interaction force, as shown in Fig. 11(c) and (d). When the particle velocity was lower than the gas velocity, the particles were accelerated by the gravitational and drag forces. However, when the particle velocity was lower, the particle-wall interaction force was lower than the particle-particle interaction force [47]. When the particle velocity was higher than the gas velocity, the larger particle-wall interaction force which was induced for a short time contacted with the high particle velocity. This led to the particle-wall interaction force becoming higher than the particle-particle interaction force. In particular, for the low strength particles, the particle-wall interaction force caused the particle breakage ratio to increase. Therefore, when the particle velocity was higher than the gas velocity, the particle-wall interaction force became the main cause of the particle breakages and wall attrition.

The cyclone pressure drop first decreased, and then remained constant with the increasing solid gas ratio. Pressure drop was always selected as the parameter to value the cyclone's performance. The pressure drop was divided into two parts: the local pressure drop in the inlet and outlet region which was caused by the friction in the separation space, and the dissipation in the vortex finder [49]. The cyclone pressure drop was affected by the cyclone's geometry [10], as well as the operational conditions [50,51].The inlet solid gas ratio was found to be one of the factors which affected the cyclone's pressure drop. Yuu et al. [52] determined that the pressure drop was reduced up to 30% even when the particle concentration was 0.2 g/m^3. There have been three types of results observed for the relationship between the

pressure drop and the solid gas ratio. Some studies have found that the cyclone pressure drop first decreased, and then remained independent with the inlet solid concentration [50,53]. Other results have indicated that the cyclone's pressure drop had a negative relationship with the solid gas ratio, and the cyclone's pressure drop decreased with the increasing of the inlet solid concentration [47,54,55]. When the inlet solid concentration was higher than 0.3 kg/m^3, the cyclone's pressure drop decreased linearly with the increasing of the inlet solids [56]. Also, some studies have shown that when there was a critical inlet solid concentration, the inlet solid concentration below the critical value, and was displayed as a "U" type [7,57–59]. The separation space became the main flow zone, and the pressure drop within the separation space played a main role. When the particle velocity was higher than that of the gas, the cyclone pressure first decreased, and then remained constant, as shown in Table 6, which is qualitatively agreed with [53]. In Case 1, diffusion played a main role in the particle turbulence (as shown in Fig. 9). A particle layer formed on the wall in the separation space, which led to gas friction, decreased gas tangential velocity, transformation of the static and dynamic pressures, and the pressure drop decreased [52,54]. For Cases 2 to 5, the width of the particle strand changed only slightly. The particle strand's turning points moved downward, which suggested that the particle moving distance became shorter, as shown in Table 6. Fig. 11 shows the particle-particle and particle-wall contact numbers. The particle residence within the cyclone increased as the solid gas ratio increased. However, the particle-particle contact number increase was larger, while the particle-wall contact numbers only showed minimal changes. All of the results showed that the particle layer thickness increased, which increased the roughness of the walls of the cyclone. When the gas velocity was low, the cyclone's pressure drop change which was induced by the increased particle layer could be neglected [60]. Therefore, it was determined that the cyclone's pressure drop first decreased, and then remained constant when the particle velocity was higher than the gas velocity.

In order to reduce the particle breakage and wall attrition in the pneumatic conveying, the pipe cross section area should be adjustable to the cyclone inlet, and only a minimal diameter change joint used. Another method would be the optimization of the diameter change joint, which would extend the diameter change joint's length, and thereby reduce the particle velocity before the particles flowed into the cyclone.

5. Conclusions

The existence of particles was found to have a high impact on the conical separation and inlet regions. The tangential, axial, and radial velocities changed only minimally with the increased solid gas ratio, when the particle velocity was higher than the gas at same gas velocity/particle velocity ratio. While the velocities increased with the increasing of gas velocity/particle velocity ratios under same solid gas ratio. The particle flow pattern formed, and then remained steady at the same gas velocity/particle velocity ratio under the different solid gas ratios. The particle strands formed early with the increasing of gas velocity/particle velocity ratios at the same solid gas ratio. The particle strand's descending distance became longer with the increased solid gas ratio. An ash top ring appeared, and became strong. The particle-wall interaction force was higher than the particle-particle interaction force at the same solid gas ratio, when the particle velocity higher was than gas velocity. It was determined that the particle-wall interaction force was the main cause of the particle breakage and wall attrition. The pressure drop first decreased with the low inlet solid gas ratio, and then remained independent of the inlet solid ratio when the inlet solid gas ratio was high. In order to reduce the particle breakage and wall attrition in the pneumatic conveying, the use of a diameter change joint or an extension of the diameter change joint's length should be avoided.

Acknowledgements:

This work was financially supported by the Fostering Foundation of the Henan Polytechnic University for Excellent PhD Dissertation (72705/006), and the Fund for Science and Technology Innovation Talents of Henan Province (NO. 164100510013). JD is supported by Australian Postgraduate Award (APA) PhD scholarship and Vice Chancellor and President's Scholarships (University of South Australia).

References

[1] P.A. Yazdabadi, A.J. Griffiths, N. Syred, Characterization of the PVC phenomena in the exhaust of a cyclone dust separator, Exp. Fluids 17 (1994) 84–95.
[2] T. O'Doherty, A.J. Griffiths, N. Syred, P.J. Bowen, W. Fick, Experimental analysis of rotating instabilities in swirling and cyclonic flows, Dev. Chem. Eng. Miner. Process. 7 (1999) 245–267.
[3] G. Solero, A. Coghe, Experimental fluid dynamic characterization of a cyclone chamber, Exp. Thermal Fluid Sci. 27 (2002) 87–96.
[4] L.Y. Hu, L.X. Zhou, J. Zhang, M.X. Shi, Studies on strongly swirling flows in the full space of a volute cyclone separator, AICHE J. 51 (2005) 740–749.
[5] S. Demir, A practical model for estimating pressure drop in cyclone separators: an experimental study, Powder Technol. 268 (2014) 329–338.
[6] R.B. Xiang, K.W. Lee, Numerical study of flow field in cyclones of different height, Chem. Eng. Process. Process Intensif. 44 (2005) 877–883.
[7] J. Chen, M. Shi, A universal model to calculate cyclone pressure drop, Powder Technol. 171 (2007) 184–191.
[8] K. Elsayed, Optimization of the cyclone separator geometry for minimum pressure drop using Co-kriging, Powder Technol. 269 (2015) 409–424.
[9] J. Oh, S. Choi, J. Kim, Numerical simulation of an internal flow field in a uniflow cyclone separator, Powder Technol. 274 (2015) 135–145.
[10] S. Demir, A. Karadeniz, M. Aksel, Effects of cylindrical and conical heights on pressure and velocity fields in cyclones, Powder Technol. 295 (2016) 209–217.
[11] H. Safikhani, P. Mehrabian, Numerical study of flow field in new cyclone separators, Adv. Powder Technol. 27 (2016) 379–387.
[12] J. Houben, C. Weiss, E. Brunnmair, S. Pirker, CFD simulations of pressure drop and velocity field in a cyclone separator with central vortex stabilization rod, J. Appl. Fluid Mech. 9 (2016) 487–499.
[13] F. Boysan, W.H. Ayers, J. Swithenbank, A fundamental mathematical modelling approach to cyclone design, Trans. Inst. Chem. Eng. 60 (1982) 222–230.
[14] G. Wan, G. Sun, X. Xue, M. Shi, Solids concentration simulation of different size particles in a cyclone separator, Powder Technol. 183 (2008) 94–104.
[15] J.J. Derksen, Separation performance predictions of a Stairmand high-efficiency cyclone, AICHE J. 49 (2003) 1359–1371.
[16] K. Elsayed, C. Lacor, Numerical modeling of the flow field and performance in cyclones of different cone-tip diameters, Comput. Fluids 51 (2011) 48–59.
[17] K. Elsayed, C. Lacor, The effect of cyclone vortex finder dimensions on the flow pattern and performance using LES, Comput. Fluids 71 (2013) 224–239.
[18] H. Shalaby, K. Pachler, K. Wozniak, G. Wozniak, Comparative study of the continuous phase flow in a cyclone separator using different turbulence models, Int. J. Numer. Methods Fluids 48 (2005) 1175–1197.
[19] M.D. Slack, R.O. Prasad, A. Bakker, F. Boysan, Advances in cyclone modelling using unstructured grids, Chem. Eng. Res. Des. 78 (2000) 1098–1104.
[20] H. Shalaby, K. Wozniak, G. Wozniak, Numerical calculation of particle-laden cyclone separator flow using Les, Eng. Appl. Comput. Fluid Mech. 2 (2008) 382–392.
[21] B.E. Launder, G.J. Reece, W. Rodi, Progress in the development of a Reynolds-stress turbulence closure, J. Fluid Mech. 68 (1975) 537–566.
[22] L.S. Brar, R.P. Sharma, K. Elsayed, The effect of the cyclone length on the performance of Stairmand high-efficiency cyclone, Powder Technol. 286 (2015) 668–677.
[23] T. Mothilal, K. Pitchandi, Influence of inlet velocity of air and solid particle feed rate on holdup mass and heat transfer characteristics in cyclone heat exchanger, J. Mech. Sci. Technol. 29 (2015) 4509–4518.
[24] T. Zhang, C. Liu, K. Guo, H. Liu, Z. Wang, Analysis of flow field in optimal cyclone separators with hexagonal structure using mathematical models and computational fluid dynamics simulation, Ind. Eng. Chem. Res. (2015).
[25] K. Elsayed, C. Lacor, The effect of cyclone inlet dimensions on the flow pattern and performance, App. Math. Model. 35 (2011) 1952–1968.
[26] J.J. Derksen, H. Van den Akker, S. Sundaresan, Two-way coupled large-eddy simulations of the gas-solid flow in cyclone separators, AICHE J. 54 (2008) 872–885.
[27] Y. Tsuji, T. Tanaka, T. Ishida, Lagrangian numerical simulation of plug flow of cohesionless particles in a horizontal pipe, Powder Technol. 71 (1992) 239–250.
[28] J. Zhao, T. Shan, Coupled CFD–DEM simulation of fluid–particle interaction in geomechanics, Powder Technol. 239 (2013) 248–258.
[29] X. Ku, T. Li, T. Løvås, CFD–DEM simulation of biomass gasification with steam in a fluidized bed reactor, Chem. Eng. Sci. 122 (2015) 270–283.
[30] S. Akhshik, M. Behzad, M. Rajabi, CFD–DEM approach to investigate the effect of drill pipe rotation on cuttings transport behavior, J. Petrol. Sci. Eng. 127 (2015) 229–244.
[31] K.W. Chu, B. Wang, A.B. Yu, A. Vince, G.D. Barnett, P.J. Barnett, CFD–DEM study of the effect of particle density distribution on the multiphase flow and performance of dense medium cyclone, Miner. Eng. 22 (2009) 893–909.
[32] M. Ebrahimi, M. Crapper, J.Y. Ooi, Numerical and experimental study of horizontal pneumatic transportation of spherical and low-aspect-ratio cylindrical particles, Powder Technol. 293 (2016) 48–59.

[33] F. Zhou, S. Hu, Y. Liu, C. Liu, T. Xia, CFD–DEM simulation of the pneumatic conveying of fine particles through a horizontal slit, Particuology 16 (2014) 196–205.
[34] C.W. Haig, A. Hursthouse, S. Mcilwain, D. Sykes, The effect of particle agglomeration and attrition on the separation efficiency of a Stairmand cyclone, Powder Technol. 258 (2014) 110–124.
[35] O. Molerus, M. Glückler, Development of a cyclone separator with new design, Powder Technol. 86 (1996) 37–40.
[36] G. Hu, Analysis and Simulation of Granual System by Dicrete Element Method Using EDEM, Wuhan University of Technology Press, 2010.
[37] A. Di Renzo, F.P. Di Maio, Comparison of contact-force models for the simulation of collisions in DEM-based granular flow codes, Chem. Eng. Sci. 59 (2004) 525–541.
[38] G.A. Bokkers, M. van Sint Annaland, J. Kuipers, Mixing and segregation in a bidisperse gas–solid fluidised bed: a numerical and experimental study, Powder Technol. 140 (2004) 176–186.
[39] A.J. Hoekstra, Gas Flow Field and Collection Efficiency of Cyclone Separators, TU Delft, Delft University of Technology, 2000.
[40] M. Azadi, M. Azadi, A. Mohebbi, A CFD study of the effect of cyclone size on its performance parameters, J. Hazard. Mater. 182 (2010) 835–841.
[41] C.B. Shepherd, C.E. Lapple, Air pollution control: a design approach, Cyclones, second ed.Woveland Press Inc., Illinois, 1939.
[42] J.A. Dirgo, Relationships Between Cyclone Dimensions and Performance, 1988.
[43] K.A. Coker, Understand cyclone design, Chem. Eng. Prog. 89 (1993) 51–55.
[44] C.J. Stairmand, The design and performance of cyclone separators, Trans. Inst. Chem. Eng 29 (1951) 356–383.
[45] F.J. De Souza, R. De Vasconcelos Salvo, D.A. De Moro Martins, Large Eddy simulation of the gas–particle flow in cyclone separators, Sep. Purif. Technol. 94 (2012) 61–70.
[46] S. Ganegama Bogodage, A.Y.T. Leung, CFD simulation of cyclone separators to reduce air pollution, Powder Technol. 286 (2015) 488–506.
[47] K.W. Chu, B. Wang, D.L. Xu, Y.X. Chen, A.B. Yu, CFD–DEM simulation of the gas–solid flow in a cyclone separator, Chem. Eng. Sci. 66 (2011) 834–847.
[48] B. Wang, D.L. Xu, K.W. Chu, A.B. Yu, Numerical study of gas–solid flow in a cyclone separator, App. Math. Model. 30 (2006) 1326–1342.
[49] M. Azadi, M. Azadi, An analytical study of the effect of inlet velocity on the cyclone performance using mathematical models, Powder Technol. 217 (2012) 121–127.
[50] F.L.s. Fassani, L. Goldstein, A study of the effect of high inlet solids loading on a cyclone separator pressure drop and collection efficiency, Powder Technol. 107 (2000) 60–65.
[51] J. Gimbun, T.G. Chuah, A. Fakhru, L. Razi, T.S.Y. Choong, The influence of temperature and inlet velocity on cyclone pressure drop: a CFD study, Chem. Eng. Process. Process Intensif. 44 (2005) 7–12.
[52] S. Yuu, T. Jotaki, Y. Tomita, K. Yoshida, The reduction of pressure drop due to dust loading in a conventional cyclone, Chem. Eng. Sci. 33 (1978) 1573–1580.
[53] X. Wu, J. Liu, X. Xu, Y. Xiao, Modeling and experimental validation on pressure drop in a reverse-flow cyclone separator at high inlet solid loading, J. Therm. Sci. 20 (2011) 343–348.
[54] A.C. Hoffmannc, A. van Santen, R.W.K. Allen, R. Clift, Effects of geometry and solid loading on the performance of gas cyclones, Powder Technol. 70 (1992) 83–91.
[55] A. Gil, L.M. Romeo, C. Cortes, Effect of the solid loading on a PFBC cyclone with pneumatic extraction of solids, Chem. Eng. Technol. 25 (2002) 407–415.
[56] S.H. Li, H. Zhang, H.R. Yang, S. Yang, J.F. Lu, G.X. Yue, Determining cyclone particle holdup by pressure drop for a CFB boiler, Chem. Eng. Technol. 30 (2007) 1726–1731.
[57] M. Trefz, E. Muschelknautz, Extended cyclone theory for gas flows with high solids concentrations, Chem. Eng. Technol. 16 (1993) 153–160.
[58] Y. Zhu, K.W. Lee, Experimental study on small cyclones operating at high flowrates, J. Aerosol Sci. 30 (1999) 1303–1315.
[59] S. Yang, H. Yang, H. Zhang, S. Li, G. Yue, A transient method to study the pressure drop characteristics of the cyclone in a CFB system, Powder Technol. 192 (2009) 105–109.
[60] I.K.A.A. Fuat Kaya, Effects of surface roughness on the performance of tangential inlet cyclone separators, Aerosol Sci. Tech. 8 (2011) 988–995.